



1 **Surface predictor of overturning circulation and heat content change in**  
2 **the subpolar North Atlantic**

3  
4 Damien. G. Desbruyères\*<sup>1</sup> ; Herlé Mercier<sup>2</sup> ; Guillaume Maze<sup>1</sup> ; Nathalie Daniault<sup>2</sup>

5  
6 1. Ifremer, University of Brest, CNRS, IRD, Laboratoire d’Océanographie Physique et  
7 Spatiale, IUEM, Ifremer centre de Bretagne, Plouzané, 29280, France

8  
9 2. University of Brest, CNRS, Ifremer, IRD, Laboratoire d’Océanographie Physique et  
10 Spatiale, IUEM, Ifremer centre de Bretagne, Plouzané, 29280, France

11 Corresponding author: Damien Desbruyères ([damien.desbruyeres@ifremer.fr](mailto:damien.desbruyeres@ifremer.fr))

12  
13 **Abstract.** The Atlantic Meridional Overturning Circulation (AMOC) impacts ocean and atmosphere  
14 temperatures on a wide range of temporal and spatial scales. Here we use observational data sets to  
15 validate model-based inferences on the usefulness of thermodynamics theory in reconstructing AMOC  
16 variability at low-frequency, and further build on this reconstruction to provide prediction of the near-  
17 future (2019-2022) North Atlantic state. An easily-observed surface quantity – the rate of warm to cold  
18 transformation of water masses at high latitudes – is found to lead the observed AMOC at 45°N by 5-6  
19 years and to drive its 1993-2010 decline and its ongoing recovery, with suggestive prediction of extreme  
20 intensities for the early 2020’s. We further demonstrate that AMOC variability drove a bi-decadal  
21 warming-to-cooling reversal in the subpolar North Atlantic before triggering a recent return to warming  
22 conditions that should prevail at least until 2021. Overall, this mechanistic approach of AMOC variability  
23 and its impact on ocean temperature brings new keys for understanding and predicting climatic conditions  
24 in the North Atlantic and beyond.

25 **1. Introduction**

26 The north-eastward meandering flow of the North Atlantic Current (NAC) dominates the upper-ocean



27 circulation of the northern North Atlantic (Krauss, 1986). It transports relatively warm waters that release  
28 heat to the atmosphere as they flow around the Subpolar Gyre (SPG) and the Nordic Seas, ultimately  
29 forming North Atlantic Deep Water that propagates in the deep layers via upper and deep western  
30 boundary currents (DWBC) and dispersive interior pathways (Bower et al., 2009; Lherminier et al., 2010,  
31 see Figure S1 for domain boundaries and bathymetric features). On top of sequestering physical and  
32 biogeochemical properties in the deep seas, the warm-to-cold conversion of water masses and the  
33 meridional overturning circulation associated with it drives a significant meridional heat transport. Its  
34 variability is thought to be a major cause of temperature and ocean heat content (OHC) shifts in the upper  
35 layer of the northern North Atlantic, with important ramification for ocean-atmosphere interactions and  
36 large-scale climate variability (Bryden et al., 2014; Robson et al., 2017). In particular, the most recent  
37 reversal of climatic trends in the north Atlantic SPG since 2005 (warming to cooling) has been attributed  
38 in numerical models to a decadal weakening of the ocean meridional heat transport across the southern  
39 boundary of the SPG (Piecuch et al., 2017; Robson et al., 2016). The recent return of intense ocean-to-  
40 atmosphere heat loss (and associated deep convection) since the mid 2010's (Josey et al., 2018;  
41 Yashayaev and Loder, 2017) is now suggestive of an ongoing or approaching re-intensification of the  
42 circulation and, consequently, a shift to warming condition in the SPG. Overall, the need for a continuous  
43 monitoring of the top-to-bottom current field in the SPG has appeared critical to capture the many  
44 components of this warm-to-cold transformation. In 2014, international efforts led to the implementation  
45 of an in situ mooring array aimed to fulfil such a need – the Overturning in the Subpolar North Atlantic  
46 Program (OSNAP; Lozier et al., 2017).

47 In the commonly-used depth space ( $z$ ), the  $AMOC_z$  streamfunction helps to simplify the complex three-  
48 dimensional velocity field of the North Atlantic into a northward flow of *about* 16 Sv ( $1 \text{ Sv} = 10^6 \text{ m}^3 \text{ s}^{-1}$ )  
49 in the upper 0-1000 m or so and a compensating southward flow at depth, connected vertically by the net  
50 sinking of surface waters at high latitudes (Buckley and Marshall, 2016; Wunsch, 2002). However, if one  
51 is interested in OHC and the dynamics of buoyancy redistribution in the ocean, an estimator of the  
52 circulation in density-space ( $\sigma$ ) must be preferred, which we will note  $AMOC_\sigma$  hereafter. Such an  
53 estimator allows to fully capture transformation of light water masses into denser ones at high latitudes,



54 along both the vertical overturning and horizontal gyre circulations (Lherminier et al., 2010; Pickart and  
55 Spall, 2007).

56 In the absence of diapycnal mixing, the diapycnal volume fluxes associated with the  $AMOC_{\sigma}$  at a given  
57 latitude must relate to air-sea exchanges of buoyancy within isopycnal outcrops north of this latitude  
58 (Figure 1). This thermodynamic balance between the  $AMOC_{\sigma}$  and its surface-forced component (noted  
59  $SFOC_{\sigma}$  hereafter), theorized by Walin (1982) and much later verified with numerical models (Grist et al.,  
60 2010; Marsh, 2000), suggests key monitoring and predictive skills of  $AMOC_{\sigma}$ . This was particularly  
61 evidenced in low-resolution coupled climate models, which hold a significant lagged relationship between  
62 high latitude surface forcing and overturning circulation at the southern exit of the SPG (Grist et al.,  
63 2009). In a follow-up paper, Grist et al. (2014) estimated the surface-forced component of the AMOC in  
64 several atmospheric reanalyses and highlighted their overall consistency in the SPG. An independent  
65 validation of those surface indices with observation-based time series of the interior circulation is  
66 however, still missing. Moreover, the potential of such proxy-based reconstruction of the AMOC for  
67 predicting OHC variability and new climatic reversal in the coming years remains to be shown.

68 The primary purposes of the present study are (1) to validate with observational data the predictive skill  
69 of surface-forced water mass transformation for AMOC variability, and (2) to assess the causal link  
70 between AMOC variability and decadal OHC changes in the SPG and perform near-future prediction of  
71 those quantities. Regional variability will also be documented, with details on the capability of the *in situ*  
72 OSNAP array in monitoring the basin-wide  $AMOC_{\sigma}$ .

73 The paper is structured as follows. Section 2 presents the observational data sets and the methodology  
74 used to compute  $AMOC_{\sigma}$ ,  $SFOC_{\sigma}$ , and OHC. Section 3 gathers the main results of the study and Section  
75 4 summarizes and discusses them.



## 76 2. Materials and Methods

### 77 2.1. Data

78 Monthly gridded potential temperature ( $\theta$ ) and practical salinity (S) profiles from four *in situ*  
79 hydrographic datasets were used. Details on those data sets (EN4, CORA, ISHII and ARMOR3D) are  
80 provide in Table S1. For each product and at each grid point, the  $\theta$  and S profiles were interpolated to a  
81 regular 20 db vertical spacing. Using the TEOS-10 Gibbs-SeaWater (GSW) toolbox, practical salinity  
82 was converted to absolute salinity, potential temperature to conservative temperature, and  $\sigma_0$  and  $\sigma_1$   
83 (potential density relative to sea-surface and 1000 m, respectively) were computed. Air-sea heat fluxes  
84 (radiative and turbulent) and freshwater fluxes (evaporation and precipitation) are obtained from three  
85 atmospheric reanalyses (NCEP2, ERA-I and CERES, see Table S1). Absolute dynamic topography and  
86 associated surface meridional geostrophic velocities are obtained from the AVISO platform  
87 (<https://www.aviso.altimetry.fr/en/data.html>) and combine sea-level anomalies from multi-mission  
88 satellite altimeters and mean dynamic topography from GOCE, GRACE, altimetry and *in situ* data  
89 (<https://www.aviso.altimetry.fr/en/data/products/auxiliary-products/mdt.html>).

90 The various quantities derived from those data products (and described below in Section 2.2 and 2.3)  
91 were then combined into ensemble mean over the period 1993-2017, with associated ensemble standard  
92 errors computed as  $\frac{\sigma}{\sqrt{N-1}}$ , where  $\sigma$  is the standard deviation and  $N = 4$  the number of data products used  
93 in the mean. This error captures the incompressible spread between all possible methods used as of today  
94 to interpolate sparse *in situ* observations. Further notes on statistical analysis of the reported results  
95 (correlation, trend error) are provided in Supplementary Information.

### 96 2.2. Computation of $AMOC_\sigma$ , $MHT_\sigma$ and associated OHC

97 The 0-2000 m absolute meridional velocities  $v$  at 45°N are derived by referencing *in situ* estimates of the  
98 geostrophic thermal-wind currents with altimetry-derived sea-surface geostrophic velocities, following  
99 previously-published methodologies (Gourcuff et al., 2011; Mercier et al., 2015; Sarafanov et al., 2012).  
100 The  $AMOC_\sigma$  stream function is then obtained by integrating  $v$  zonally and vertically above each  $\sigma_1$



101 surface (spaced by  $\delta\sigma = 0.025 \text{ kg m}^{-3}$ ). The maximum value of the resulting stream function at the density  
 102 level  $\sigma_m$  writes as:

$$103 \quad AMOC_{\sigma_m} = \int_x \int_{\sigma < \sigma_m} v dx dz$$

104

105 We restrict such calculation to the 0-2000 m layer as not all products contain data below that depth<sup>1</sup>. This  
 106 threshold is nonetheless deep enough to capture the level of maximum transformation at 45°N, as well as  
 107 its variability. The  $AMOC_{\sigma}$ -driven heat transport is estimated as in Mercier et al. (2015):

108

$$109 \quad MHT_{\sigma} = \rho_0 C_p \max(AMOC_{\sigma}) \Delta \theta$$

110

111 Where  $\rho_0 = 1025 \text{ kg m}^{-3}$ ,  $C_p = 4000 \text{ J kg}^{-1} \text{ }^{\circ}\text{C}^{-1}$  and  $\Delta \theta$  is the temperature difference between the upper  
 112 and lower limbs of the  $AMOC_{\sigma}$  (i.e. the area-weighted average temperature of water lighter than  $\sigma_m$  minus  
 113 the area-weighted average temperature of water heavier than  $\sigma_m$ ). Note that  $\Delta \theta$  was computed from the  
 114 EN4.2.0 product that provides full-depth temperature profiles. The change in ocean heat content north of  
 115 45°N driven by  $MHT_{\sigma}$  is then estimated as:

$$116 \quad OHC(t)_{MHT_{\sigma}} = \int_{t_0}^t (MHT(t)_{\sigma} - \overline{MHT_{\sigma}}) dt$$

117 where  $t$  is a given year and the overbar refers to a temporal average over the period 1996 – 2013. This  
 118 reference period is assumed to represent a climatological equilibrium state around which  
 119  $MHT_{\sigma}$  fluctuates, so that positive (negative) anomalies in  $MHT_{\sigma}$  result in warming (cooling) north of  
 120 45°N. As shown in Section 3.3, this assumption yields high and significant correlation between  
 121  $OHC_{MHT_{\sigma}}$  and the observed OHC in the SPG.

122

---

<sup>1</sup> This is due to the fact that the main source of recent in situ data is the Argo array of profiling floats (Riser et al., 2016) providing quality controlled temperature and salinity data for the upper 2000m only.



123 **2.3. Computation of  $SFOC_{\sigma}$ .**

124 The surface-forced component of the overturning streamfunction  $SFOC_{\sigma}$  was computed following  
125 common practice and methodologies (Marsh, 2000). For each month and each isopycnal  $\sigma$  (spaced by  $\delta\sigma$   
126 = 0.05 kg m<sup>-3</sup>),  $SFOC_{\sigma}$  is computed as the diapycnal convergence of the diapycnal volume flux driven by  
127 surface density flux wherever  $\sigma$  outcrops north of a given coast-to-coast section:

128

129 
$$SFOC(\sigma^*) = \frac{1}{\delta\sigma} \iint \left[ -\frac{\alpha Q}{C_p} + \beta \frac{S}{1-S} (E - P) \right] \Pi(\sigma) dx dy$$

130 where

131 
$$\Pi(\sigma) = \begin{cases} 1 & \text{for } \sigma - \frac{\delta\sigma}{2} < \sigma < \sigma + \frac{\delta\sigma}{2} \\ 0 & \text{elsewhere} \end{cases}$$

132

133 The quantity within brackets is the local surface density flux,  $\alpha$  and  $\beta$  are the thermal expansion and  
134 haline contraction coefficients,  $C_p$  is specific heat capacity of sea water (4000 J kg<sup>-1</sup> K<sup>-1</sup>),  $Q$  the net  
135 surface heat flux,  $E$  the evaporation rate, and  $P$  the precipitation rate. Following Marsh (2000), monthly  
136 fields of surface  $\theta$  and  $Q$  are used herein while monthly climatology values for surface  $S$  and  $E - P$  are  
137 used. When for a given month (usually during summer),  $\sigma$  does not outcrop north of 45°N,  $SFOC_{\sigma}$  is set  
138 to zero. Annual averages are then obtained for 1985-2017. Even if  $SFOC_{\sigma}$  is a surface integral statement,  
139 maps of transformation rates can be obtained by accumulating the integrand over outcrops (Brambilla et  
140 al., 2008; Maze et al., 2009), as shown later in Section 3.1.

141

142 In order to directly relate  $SFOC_{\sigma}$  and  $AMOC_{\sigma}$ , we rely on the assumption of water mass steadiness in the  
143 SPG, meaning that the net accumulation of volume within isopycnal layers is considered to be negligible  
144 in front of the import of light water to be transformed and the export of dense water after transformation  
145 (Marsh, 2000). To verify this hypothesis, we compute  $\frac{dV_{\sigma}}{dt}$ , the yearly local change in the volume of  
146 discrete isopycnal layer (in Sv), where  $V_{\sigma}$  is evaluated on January 1<sup>st</sup> of each year. Averaging this term



147 north of 45°N and summing below the density level of maximum SFOC<sub>σ</sub> yields an evaluation of water  
 148 mass steadiness during each year. As discussed later, this term can be intermittently important but does  
 149 not dominate the decadal variability, so that a direct link emerges between SFOC<sub>σ</sub> and AMOC<sub>σ</sub> on those  
 150 relatively long-time scales.

151

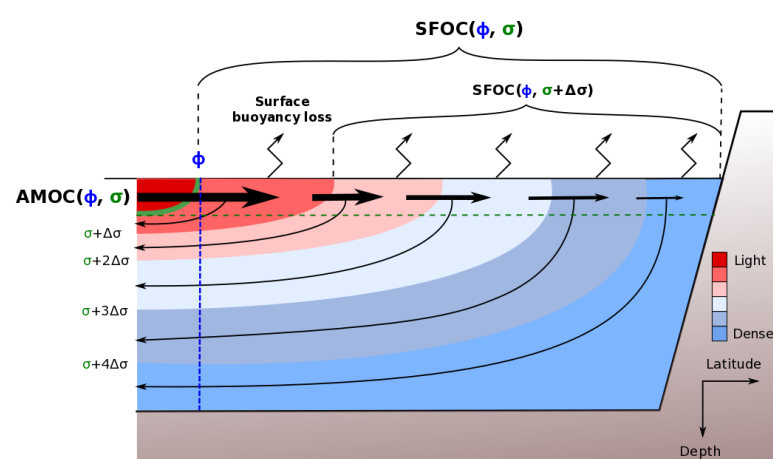


**Figure 1.** Schematic of the relationship between meridional overturning circulation at latitude  $\phi$  and isopycnal surface  $\sigma$  – the  $AMOC(\phi, \sigma)$  – and its surface-forced component – the  $SFOC(\phi, \sigma)$ . Arrows show the progressive transformation of waters across increasing density surfaces balanced by buoyancy loss at the air-sea interface and meridional import and export. After Marsh (2000).

152

### 153 3. Results

#### 154 3.1. The time-mean AMOC<sub>σ</sub> and SFOC<sub>σ</sub>

155 The time-mean depth-longitude field of meridional velocity at 45°N (Figure 2A) is dominated by a  
 156 western boundary current system in good quantitative agreement with direct current estimates carried out  
 157 in the region (Mertens et al., 2014; Toole et al., 2017). This current system includes the southward-  
 158 flowing Labrador Current (LC) adjacent to the slope above 800 m (16 Sv), the upper part of the  
 159 southward-flowing DWBC circa 47°W with increasing velocities with depth (13 Sv), and the surface-



160 intensified northward-flowing NAC (53 Sv) with its recirculation east of 45°W (28 Sv). Meridional  
161 velocities are significantly weaker further east in the gyre interior. Integrating zonally the volume  
162 transport above discrete  $\sigma_1$ -surfaces yields the (partial)  $\text{AMOC}_\sigma$  stream function at 45°N, which reaches  
163 a time-mean maximum value of  $14.3 \pm 1.4$  Sv at  $\sigma_1 = 32.15$  (Figure 2B; see also Figure S2A for the  
164  $\text{AMOC}_\sigma$  stream function of each individual product). A similar calculation in depth space yields the  
165 (partial)  $\text{AMOC}_z$  stream function at 45°N, which reaches a time-mean maximum value of  $9 \pm 0.4$  Sv at  
166 700 m depth (Figure S2B). Therefore, about 60% of the maximum diapycnal volume flux above 2000 m  
167 depth at 45°N is associated with a net downwelling in the vertical plane, the remainder being due to dense  
168 waters returning at the same depth as that of the inflowing light waters within the horizontal gyre  
169 circulation.

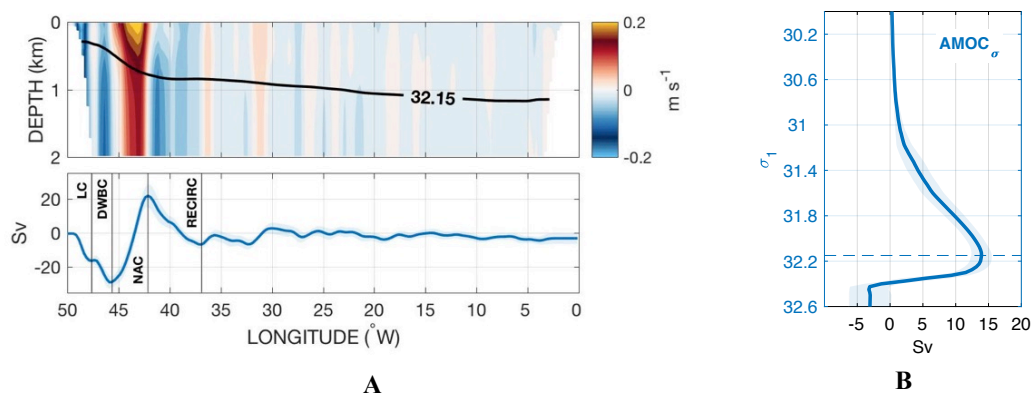


**Figure 2. Meridional velocity and transport at 45°N ( $\text{AMOC}_\sigma$ ).** (A) Top: The mean longitude-depth velocity field (in  $\text{m s}^{-1}$ ) at 45°N. The  $\sigma_1 = 32.15$  isopycnal across which the maximum diapycnal flux occurs is shown in black. Bottom: The depth-integrated (0-2000 m) zonally cumulated transport (in Sv) at 45°N, with labels as follow: LC (Labrador Current), DWBC (Deep Western Boundary Current), NAC (North Atlantic Current) and RECIRC (NAC recirculation). Shading indicates the ensemble standard error. (B). The mean  $\text{AMOC}_\sigma$  streamfunction at 45°N (in Sv). Shading indicates the ensemble standard error. The blue dashed line at  $\sigma_1 = 32.15$  depicts the maximum transformation rate.





170 The surface-forced component of the  $AMOC_{\sigma}$  (noted  $SFOC_{\sigma}$ ) shows a maximum time-mean value of  
171  $15.4 \pm 1.8$  Sv at  $\sigma_0 = 27.4$  (or  $\sigma_1 \approx 32$ ), which reflects a light-to-dense flux that primarily occurs along the  
172 NAC path in the eastern SPG south of Reykjanes Ridge and to a lesser extent along the western SPG  
173 boundary (Labrador Sea), along the Norwegian margins (Figure 3). The spatial distribution of the surface-  
174 forced diapycnal volume flux within the domain is inferred by evaluating  $SFOC_{\sigma}$  at two additional key  
175 sections: the international Canada-Greenland-Scotland OSNAP and the Greenland-Iceland-Scotland  
176 (GIS) sills. The  $SFOC_{\sigma}^{OSNAP}$  and  $SFOC_{\sigma}^{GIS}$  stream functions respectively show a maximum  
177 transformation rate of  $11.2 \pm 1.3$  Sv at  $\sigma_0 = 27.52$  and  $5.4 \text{ Sv} \pm 0.4 \text{ Sv}$  at  $\sigma_0 = 27.77$ , in good agreement  
178 with independent *in situ* calculations of the maximum overturning across the OSNAP line and overflow  
179 transport estimates at the GIS (Hansen and Østerhus, 2000; Li et al., 2017). Altogether, the three estimates  
180 of  $SFOC_{\sigma}$  across  $45^{\circ}\text{N}$ , OSNAP, and GIS, describe the expected decrease in intensity and increase in  
181 density of the maximum transformation rate as one progress northward. We note that the density level of  
182 the maximum  $SFOC_{\sigma}$  at  $45^{\circ}\text{N}$  is slightly lighter than the density level of the maximum  $AMOC_{\sigma}$  at  $45^{\circ}\text{N}$ .  
183 This is because  $SFOC_{\sigma}$  cannot account for the positive transformation rate due to the entrainment-driven  
184 mixing of the subpolar mode waters with the denser overflow waters in the vicinity of the GIS sills.  
185 However, the analysis of numerical simulations shows that such a mixing contribution does not largely  
186 affect interannual and decadal variability (Marsh et al., 2005), our primary purpose here.

187

188

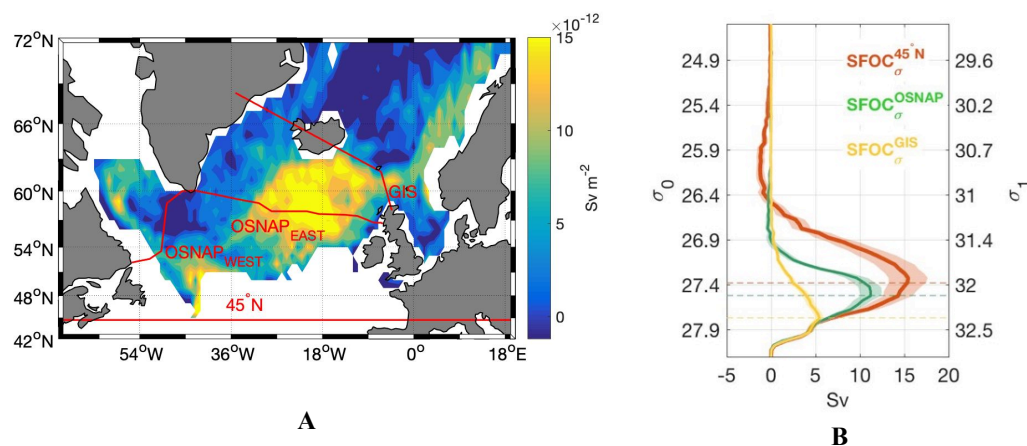


**Figure 3. The surface-forced transformation north of 45°N (SFOC<sub>σ</sub>).** (A) The time-mean transformation map across the isopycnal surface  $\sigma_0 = 27.4$  (in  $\text{Sv m}^{-2}$ ), across which the maximum transformation rate north of 45°N occurs. (B) The mean SFOC<sub>σ</sub> streamfunction (in Sv) at 45°N (red), at the OSNAP line (green) and at the GIS sills (yellow). See 5A) for section locations. Shading indicates the ensemble standard error. The dashed lines depict the density levels of maximum surface-forced transformation rate north for each domain. As the computation was made using  $\sigma_0$ , the corresponding surface  $\sigma_1$  values are shown on the right-hand side y-axis. The surface integral of the diapycnal volume flux shown in (A) yields the maximum transformation rate through  $\sigma_0 = 27.4$ :  $15.4 \pm 1.8 \text{ Sv}$ .

189

### 190 3.2. The variability of AMOC<sub>σ</sub> and SFOC<sub>σ</sub>

191 The maximum AMOC<sub>σ</sub> time series, displayed as raw and 7-year low-pass filtered annual anomalies in  
 192 Figure 4A (blue lines), shows a dominant 8-year period variability embedded in a linear decrease during  
 193 1993-2010 of  $-0.24 \pm 0.05 \text{ Sv yr}^{-1}$  and a subsequent intensification during 2010-2017 of  $0.91 \pm 0.19 \text{ Sv}$   
 194  $\text{yr}^{-1}$ . Those changes are largely advective (Figure S3), indicating minor impact of volume (or  $\sigma_m$ )  
 195 variability on the AMOC intensity. Volume redistribution associated with the formation history of  
 196 intermediate water masses in the Labrador and Irminger seas can be important but they remain restricted  
 197 to the lower limb of the AMOC<sub>σ</sub> (not shown). We note that the AMOC<sub>Z</sub> shares a similar variability with  
 198 AMOC<sub>σ</sub> but of weaker amplitude, indicating an important contribution of the horizontal circulation  
 199 (versus vertical overturning) to the diapycnal volume flux variability at 45°N (Figure S3). The gyre



200 contribution to  $AMOC_{\sigma}$  variability at  $45^{\circ}N$  is also inferred from an independent mooring-based  
201 observation of the (400m-bottom) DWBC intensity at  $53^{\circ}N$  (Zantopp et al., 2017). Although the shortness  
202 of the time series (10 years) only allows a suggestive independent validation, the DWBC variability is  
203 found to consistently lead the 2004-2010 weakening and the 2010-2014 intensification of the  $AMOC_{\sigma}$  at  
204  $45^{\circ}N$  by 3 years (Figure S3).

205

206 The second independent validation of  $AMOC_{\sigma}$  bears the mechanistic explanation of its variability. While  
207 the maximums of  $AMOC_{\sigma}$  and  $SFOC_{\sigma}$  hardly correlate at high frequency, a striking correspondence  
208 between their low-pass filtered variability is found, with the largest correlation obtained when the former  
209 lags the latter by 5-6 years (0.94 at the 99% confidence level), in line with typical advective time scales  
210 in the SPG (Bersch et al., 2007) (Figure 4A – see also Supplementary Materials for details on smoothing  
211 and correlation). Therefore, observational data confirm that surface-forced water mass transformation  
212 represents a dominant driver as well as an easily-derived proxy of low-frequency  $AMOC_{\sigma}$  changes across  
213 the southern exit of the SPG. Departure from an exact match between  $AMOC_{\sigma}$  and  $SFOC_{\sigma}$  relate to the  
214 influence of the remaining terms in the volume budget equation, namely diapycnal mixing and volume  
215 storage within the SPG interior. As shown in Figure S4, the latter can be non-negligible on interannual  
216 time scale but exhibits minor decadal variability.

217

218 The 5-year time lag between  $AMOC_{\sigma}$  and  $SFOC_{\sigma}$  time series enables prediction of near-future  $AMOC_{\sigma}$   
219 variability. Here, the low-frequency strengthening of the meridional circulation observed since 2010 is  
220 found to continue at a similar rate until 2022 while reaching extreme intensities in 2019 and 2020 similar  
221 to those observed in the early 1990's. Those extreme events reflect harsh atmospheric winter conditions  
222 in the SPG in 2014 and 2015 (North Atlantic Oscillation strongly positive) associated with large ocean-  
223 to-atmosphere heat transfer (Josey et al., 2018). As discussed in the next section, this most recent positive  
224 trend in  $AMOC_{\sigma}$  intensity and its predicted persistence until the early 2020's may substantially increase  
225 OHC in the SPG in the coming years.

226

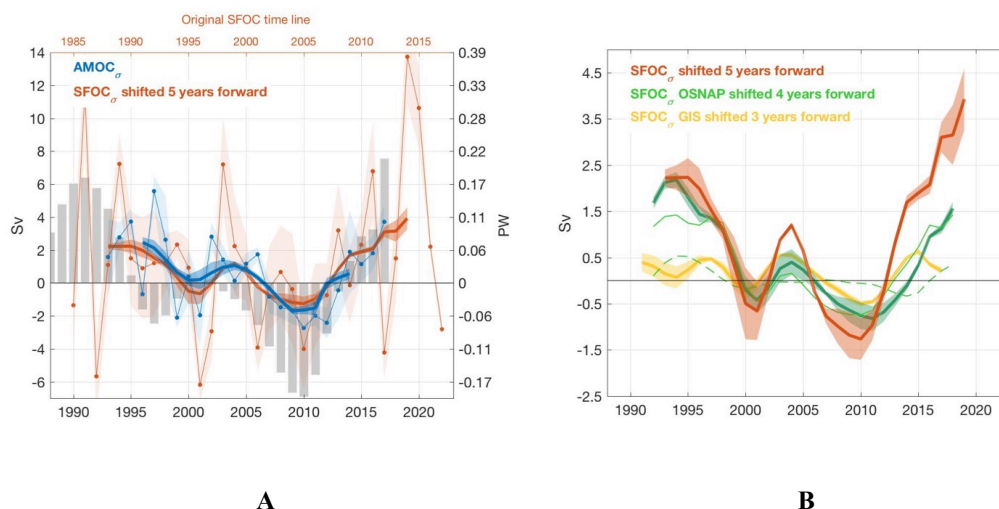


**Figure 4. The AMOC<sub>σ</sub> and SFOC<sub>σ</sub>.** (A) Annual anomalies in the maximum AMOC<sub>σ</sub> (blue) and the maximum SFOC<sub>σ</sub> (red) at 45°N (in Sv), with the latter shifted 5 years forward (lag of maximum correlation). The reference (time-mean) period is 1996–2013. Thick lines show 7-year low-pass filtered time series. The right-hand side axis displays the corresponding heat transport anomalies. The original time line for SFOC<sub>σ</sub> is given in the top x-axis. (B) The 7-year low-pass filtered time series of anomalies in the maximum SFOC<sub>σ</sub> at 45°N (red – shifted 5 years forward), the maximum SFOC<sub>σ</sub> at the OSNAP line (green – shifted 4 years forward) decomposed into contributions from the eastern (thin) and western (dashed) basins, and the maximum SFOC<sub>σ</sub> at the GIS sills (yellow – shifted 3 years forward).

227

228 The decadal variability in the maximum SFOC<sub>σ</sub> at 45°N has minor contribution from the Nordic Seas and  
 229 is effectively captured by SFOC<sub>σ</sub><sup>OSNAP</sup>, although the contribution from regions south of the OSNAP line  
 230 appears important during its most recent intensification since 2010 (Figure 4B). The variability in SFOC<sub>σ</sub>  
 231 is dominated by changes in the rate of water mass transformation in the eastern SPG basins, in line with  
 232 recent mooring-based estimates of the AMOC<sub>σ</sub> across the OSNAP line (Lozier et al., 2019). The  
 233 successive 1-year lag between SFOC<sub>σ</sub> at 45°N, SFOC<sub>σ</sub> at OSNAP and SFOC<sub>σ</sub> at GIS reflects the  
 234 progressive northward spreading of transformation anomalies across surface of increasing density (see  
 235 Figure 3B).

236



### 237           **3.3. The variability of OHC and its 5-year prediction**

238   The lagged correlation between surface-forced water mass transformation and the overturning circulation  
239   has important ramifications for the monitoring of past, present and future fluctuations of  $AMOC_{\sigma}$  but  
240   does not inform on its role in driving decadal OHC variability in the SPG. To infer such a role, the  
241    $AMOC_{\sigma}$ -driven meridional heat transport at  $45^{\circ}N$  – noted  $MHT_{\sigma}$  hereafter – is computed from the  
242   maximum  $AMOC_{\sigma}$  index (Figure 4A) and the temperature difference between the upper and lower  
243    $AMOC_{\sigma}$  limbs at  $45^{\circ}N$  (see Section 2.2). The time-mean  $MHT_{\sigma}$  at  $45^{\circ}N$  during 1993-2017 reaches  $0.43$   
244    $\pm 0.04$  PW and is balanced by an ocean-to-atmosphere heat transfer of  $0.21 \pm 0.04$  PW, a small long-term  
245   change in OHC within the SPG domain of  $0.014 \pm 0.002$  PW, and a northward ocean heat transport across  
246   the GIS sills estimated as a residual as  $0.20$  PW (consistent with independent estimates, Curry et al., 2011;  
247   Hansen et al., 2015; Hansen & Østerhus, 2000).

248

249   The cumulated anomalies of  $MHT_{\sigma}$  referenced to the time-window 1996-2013 show high correlation with  
250   the observed OHC within the 0-1000 m layer of the SPG ( $10^{\circ}W$ - $70^{\circ}W$ ;  $45^{\circ}N$ - $65^{\circ}N$ , Figure 5). In  
251   particular, both the 1993-2006 warming and the 2006-2013 cooling of the region are well explained by  
252   the contribution of  $MHT_{\sigma}$  variability at  $45^{\circ}N$  ( $r = 0.87$  at the 99% confidence level for 1993-2013). This  
253   is consistent with previous model-based inferences that the  $AMOC_{\sigma}$  is a primary driver of decadal  
254   temperature changes in the upper SPG (Desbruyères et al., 2015; Grist et al., 2010; Robson et al., 2016).  
255   This causal relationship is however not verified during 2013-2015, where  $MHT_{\sigma}$  induces a warming of  
256   the SPG whereas *in situ* observations indicate that OHC continued to decrease. This apparent discrepancy  
257   reflects the strong air-sea heat flux anomaly that drove a sharp cooling of the upper SPG during those  
258   years – the so-called “Cold blob” (Duchez et al., 2016; Josey et al., 2018). From 2015, atmospheric  
259   conditions were back to “normal” and the  $MHT_{\sigma}$ -driven warming of the SPG could begin.

260

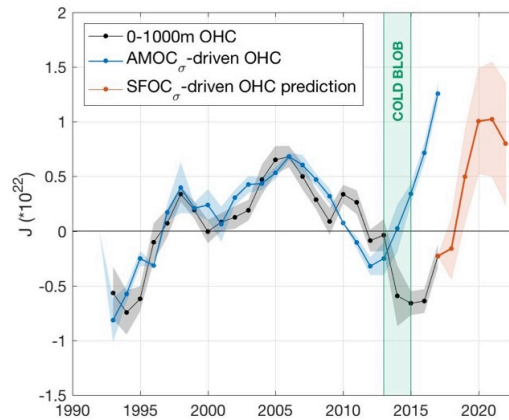


**Figure 5. OHC variability.** Detrended anomalies in OHC within the upper SPG (0-1000 m; 10°W-70°W; 45°N-65°N, black, in J) and MHT<sub>σ</sub>-driven OHC anomalies north of 45°N (blue, in J). Shading indicates the ensemble standard errors for each variable. The SFOC<sub>σ</sub>-driven OHC prediction for 2017-2022 is shown in red, with its associated error based on the historical predictive skills of SFOC<sub>σ</sub>. The green patch indicates the “cold blob” era driven by extreme air-sea flux events (Josey et al., 2018).

261

262 We finally make use of the remarkable 5-year lead of SFOC<sub>σ</sub> onto AMOC<sub>σ</sub> (Figure 4A) to make a  
 263 suggestive prediction of AMOC<sub>σ</sub>-driven OHC changes between 2017 and 2022. Annually-averaged  
 264 anomalies of SFOC<sub>σ</sub> are scaled by the actual interannual variance of AMOC<sub>σ</sub> and converted into an  
 265 anomalous heat transport relative to 1996-2013 with associated OHC anomalies as previously shown. To  
 266 make the prediction, we simply anchor the resulting 2017-2022 time series to the last observed OHC  
 267 value of 2017 (red line, Figure 5). An uncertainty is added on the prediction based on the skill of SFOC<sub>σ</sub>  
 268 in predicting the historical 1993-2017 OHC (red shading in Figure 5). This uncertainty is the prediction  
 269 error  $\epsilon_{lag}$  from the  $N_{lag}$ -year time series, with  $lag = 1$  to 5 years:

270

$$271 \quad \epsilon_{lag} = \sqrt{\frac{1}{N_{lag}} \sum \{ (OHC^{y+lag} - OHC^y) - (OHC_{SFOC\sigma}^{y+lag} - (OHC_{SFOC\sigma}^y)) \}^2}$$

272



273 Owing to the ongoing intensification of the AMOC<sub>σ</sub> and its presumed persistence until 2019/2020 (Figure  
274 4A), and under the (hypothesized) absence of extreme air-sea heat flux events in the near-future, the  
275 present analysis predicts a rapid OHC surge of  $1.03 \pm 0.57 \cdot 10^{22}$  J between 2017 and 2021 (Figure 5).

276

#### 277 **4. Conclusions**

278 In this paper we have provided observationally-based evidence of a tight causal relationship between low  
279 frequency changes in the rate of surface-forced water mass transformation in the eastern SPG, the  
280 variability of the overturning circulation at 45°N, and ocean heat content trends in the SPG. The 5-year  
281 delay between surface property changes in the SPG and downstream circulation changes suggests good  
282 skills for short-term predictability in the region from the sole use of ocean surface and air-sea interface  
283 measurements. Here, a strong intensification of the overturning and associated heat transport from 2010  
284 is found to persist until the early 2020's, driving a new significant reversal of climatic condition in the  
285 SPG as temperature rapidly rise from their last minimum of 2017. The extreme winters of 2014 and 2015  
286 appear as key drivers of those recent and upcoming changes in the SPG. They are found to be responsible  
287 for rapidly cooling the upper ocean while feeding a 5-year delayed intensification of the overturning  
288 through increased light-to-dense transformation, leading eventually to a sharp warming of the domain.  
289 We finally note that the series of oceanic events described herein, from surface-forced water mass  
290 transformation to meridional circulation and heat content changes, are only suggestively presented as a  
291 forced response to atmospheric variability. Understanding the extent to which they may belong to a more  
292 complex loop of coupled ocean-atmosphere interactions is beyond the scope of the present study.

293

#### 294 **Acknowledgments**

295 DD and GM were supported by Ifremer. HM was supported by CNRS. ND was supported by University  
296 of Brest. DD carried out the data analysis. This work was supported by the french national programme  
297 LEFE/INSU: OBLADY and SOMOVAR, leded by DD and GM, respectively. All authors contributed



298 to the interpretation, description and presentation of the results. All datasets used herein are available  
299 online (see Supplementary Information for references).

300

### 301 **References**

302 Bersch, M., Yashayaev, I. and Koltermann, K. P.: Recent changes of the thermohaline circulation in the  
303 subpolar North Atlantic, *Ocean Dyn.*, 57(3), 223–235, doi:10.1007/s10236-007-0104-7, 2007.

304

305 Bower, A. S., Lozier, M. S., Gary, S. F. and Böning, C. W.: Interior pathways of the North Atlantic  
306 meridional overturning circulation, *Nature*, 459(7244), 243–247, doi:10.1038/nature07979, 2009.

307

308 Brambilla, E., Talley, L. D. and Robbins, P. E.: Subpolar mode water in the northeastern Atlantic: 2.  
309 Origin and transformation, *J. Geophys. Res. Ocean.*, 113(4), 1–16, doi:10.1029/2006JC004063, 2008.

310

311 Bryden, H. L., King, B. A., McCarthy, G. D. and McDonagh, E. L.: Impact of a 30% reduction in Atlantic  
312 meridional overturning during 2009-2010, *Ocean Sci.*, 10(4), 683–691, doi:10.5194/os-10-683-2014,  
313 2014.

314 Buckley, M. W. and Marshall, J.: Observations, inferences, and mechanisms of the Atlantic Meridional  
315 Overturning Circulation: A review, *Rev. Geophys.*, 54(1), 5–63, doi:10.1002/2015RG000493, 2016.

316

317 Curry, B., Lee, C. M. and Petrie, B.: Volume, Freshwater, and Heat Fluxes through Davis Strait, 2004–  
318 05\*, *J. Phys. Oceanogr.*, 41(3), 429–436, doi:10.1175/2010JPO4536.1, 2011.

319

320 Desbruyères, D., Mercier, H. and Thierry, V.: On the mechanisms behind decadal heat content changes  
321 in the eastern subpolar gyre, *Prog. Oceanogr.*, 132, 262–272, doi:10.1016/j.pocean.2014.02.005, 2015.

322

323 Duchez, A., Frajka-Williams, E., Josey, S. A., Evans, D. G., Grist, J. P., Marsh, R., McCarthy, G. D.,  
324 Sinha, B., Berry, D. I. and Hirschi, J. J.-M.: Drivers of exceptionally cold North Atlantic Ocean





325 temperatures and their link to the 2015 European heat wave, *Environ. Res. Lett.*, 11(7), doi:10.1088/1748-  
326 9326/11/7/074004, 2016.

327

328 Gourcuff, C., Lherminier, P., Mercier, H. and Le Traon, P. Y.: Altimetry combined with hydrography for  
329 ocean transport estimation, *J. Atmos. Ocean. Technol.*, 28(10), 1324–1337,  
330 doi:10.1175/2011JTECHO818.1, 2011.

331

332 Grist, J. P., Marsh, R. and Josey, S. A.: On the Relationship between the North Atlantic Meridional  
333 Overturning Circulation and the Surface-Forced Overturning Streamfunction, , 4989–5002,  
334 doi:10.1175/2009JCLI2574.1, 2009.

335

336 Grist, J. P., Josey, S. A., Marsh, R., Good, S. A., Coward, A. C., De Cuevas, B. A., Alderson, S. G., New,  
337 A. L. and Madec, G.: The roles of surface heat flux and ocean heat transport convergence in determining  
338 Atlantic Ocean temperature variability, *Ocean Dyn.*, 60(4), 771–790, doi:10.1007/s10236-010-0292-4,  
339 2010.

340

341 Grist, J. P., Josey, S. A., Marsh, R., Kwon, Y. O., Bingham, R. J. and Blaker, A. T.: The surface-forced  
342 overturning of the North Atlantic: Estimates from modern era atmospheric reanalysis datasets, *J. Clim.*,  
343 27(10), 3596–3618, doi:10.1175/JCLI-D-13-00070.1, 2014.

344

345 Hansen, B. and Østerhus, S.: North Atlantic-Nordic Seas exchanges, *Prog. Oceanogr.*, 45(2), 109–208,  
346 doi:10.1016/S0079-6611(99)00052-X, 2000.

347

348 Hansen, B., Larsen, K. M. H., Hátún, H., Kristiansen, R., Mortensen, E. and Østerhus, S.: Transport of  
349 volume, heat, and salt towards the Arctic in the Faroe Current 1993–2013, *Ocean Sci.*, 11(5), 743–757,  
350 doi:10.5194/os-11-743-2015, 2015.

351



352 Josey, S. A., Hirschi, J. J.-M., Sinha, B., Duchez, A., Grist, J. P. and Marsh, R.: The Recent Atlantic Cold  
353 Anomaly: Causes, Consequences, and Related Phenomena, *Ann. Rev. Mar. Sci.*, 10(1), 475–501,  
354 doi:10.1146/annurev-marine-121916-063102, 2018.

355

356 Krauss, W.: The North Atlantic Current, *J. Geophys. Res.*, 91(C4), 5061–5074,  
357 doi:10.1029/JC091iC04p05061, 1986.

358

359 Lherminier, P., Mercier, H., Huck, T., Gourcuff, C., Perez, F. F., Morin, P., Sarafanov, A. and Falina, A.:  
360 The Atlantic Meridional Overturning Circulation and the subpolar gyre observed at the A25-OVIDE  
361 section in June 2002 and 2004, *Deep. Res. Part I Oceanogr. Res. Pap.*, 57(11), 1374–1391,  
362 doi:10.1016/j.dsr.2010.07.009, 2010.

363

364 Li, F., Lozier, M. S. and Johns, W. E.: Calculating the meridional volume, heat, and freshwater transports  
365 from an observing system in the subpolar North Atlantic: Observing system simulation experiment, *J.*  
366 *Atmos. Ocean. Technol.*, 34(7), 1483–1500, doi:10.1175/JTECH-D-16-0247.1, 2017.

367

368 Lozier, M. S., Bacon, S., Bower, A. S., Cunningham, S. A., De Jong, M. F., De Steur, L., De Young, B.,  
369 Fischer, J., Gary, S. F., Greenan, B. J. W., Heimbmbach, P., Holliday, N. P., Houpert, L., Inall, M. E.,  
370 Johns, W. E., Johnson, H. L., Karstensen, J., Li, F., Lin, X., Mackay, N., Marshall, D. P., Mercier, H.,  
371 Myers, P. G., Pickart, R. S., Pillar, H. R., Straneo, F., Thierry, V., Weller, R. A., Williams, R. G., Wilson,  
372 C., Yang, J., Zhao, J. and Zika, J. D.: Overturning in the Subpolar north Atlantic program: A new  
373 international ocean observing system, *Bull. Am. Meteorol. Soc.*, 98(4), 737–752, doi:10.1175/BAMS-D-  
374 16-0057.1, 2017.

375

376 Lozier, M. S., Li, F., Bacon, S., Bahr, F., Bower, A. S., Cunningham, S. A., de Jong, M. F., de Steur, L.,  
377 deYoung, B., Fischer, J., Gary, S. F., Greenan, B. J. W., Holliday, N. P., Houk, A., Houpert, L., Inall, M.  
378 E., Johns, W. E., Johnson, H. L., Johnson, C., Karstensen, J., Koman, G., Le Bras, I. A., Lin, X., Mackay,



379 N., Marshall, D. P., Mercier, H., Oltmanns, M., Pickart, R. S., Ramsey, A. L., Rayner, D., Straneo, F.,  
380 Thierry, V., Torres, D. J., Williams, R. G., Wilson, C., Yang, J., Yashayaev, I. and Zhao, J.: A sea change  
381 in our view of overturning in the subpolar North Atlantic, *Science* (80-. ), 363(6426), 516 LP-521,  
382 doi:10.1126/science.aau6592, 2019.

383

384 Marsh, R.: Recent variability of the North Atlantic thermohaline circulation inferred from surface heat  
385 and freshwater fluxes, *J. Clim.*, 13(18), 3239–3260, doi:10.1175/1520-  
386 0442(2000)013<3239:RVOTNA>2.0.CO;2, 2000.

387

388 Marsh, R., Josey, S. a., Nurser, a. J. G., de Cuevas, B. a. and Coward, a. C.: Water mass transformation  
389 in the North Atlantic over 1985–2002 simulated in an eddy-permitting model, *Ocean Sci.*, 1, 127–144,  
390 doi:10.5194/osd-2-63-2005, 2005.

391

392 Maze, G., Forget, G., Buckley, M., Marshall, J. and Cerovecki, I.: Using Transformation and Formation  
393 Maps to Study the Role of Air–Sea Heat Fluxes in North Atlantic Eighteen Degree Water Formation, *J.*  
394 *Phys. Oceanogr.*, 39(8), 1818–1835, doi:10.1175/2009JPO3985.1, 2009.

395

396 Mercier, H., Lherminier, P., Sarafanov, A., Gaillard, F., Daniault, N., Desbruyères, D., Falina, A., Ferron,  
397 B., Gourcuff, C., Huck, T. and Thierry, V.: Variability of the meridional overturning circulation at the  
398 Greenland-Portugal OVIDE section from 1993 to 2010, *Prog. Oceanogr.*, 132, 250–261,  
399 doi:10.1016/j.pocean.2013.11.001, 2015.

400

401 Mertens, C., Rhein, M., Walter, M., Böning, Claus, W., Behrens, E., Kieke, D., Steinfeldt, R. and Stöber,  
402 U.: Circulation and transports in the Newfoundland Basin, western subpolar North Atlantic, *J. Geophys.*  
403 *Res. Ocean.*, 119, 7772–7793, doi:10.1002/2014JC010019.Received, 2014.

404

405 Pickart, R. S. and Spall, M. A.: Impact of Labrador Sea Convection on the North Atlantic Meridional



- 406 Overturning Circulation, *J. Phys. Oceanogr.*, 37(9), 2207–2227, doi:10.1175/JPO3178.1, 2007.
- 407
- 408 Piecuch, C. G., Ponte, R. M., Little, C. M., Buckley, M. W. and Fukumori, I.: Mechanisms underlying  
409 recent decadal changes in subpolar North Atlantic Ocean heat content, *J. Geophys. Res. Ocean.*, (Figure  
410 1), 1–17, doi:10.1002/2017JC012845, 2017.
- 411
- 412 Riser, S. C., Freeland, H. J., Roemmich, D., Wijffels, S., Troisi, A., Belbéoch, M., Gilbert, D., Xu, J.,  
413 Pouliquen, S., Thresher, A., Le Traon, P. Y., Maze, G., Klein, B., Ravichandran, M., Grant, F., Poulain,  
414 P. M., Suga, T., Lim, B., Sterl, A., Sutton, P., Mork, K. A., Vélez-Belchí, P. J., Ansorge, I., King, B.,  
415 Turton, J., Baringer, M. and Jayne, S. R.: Fifteen years of ocean observations with the global Argo array,  
416 *Nat. Clim. Chang.*, 6(2), 145–153, doi:10.1038/nclimate2872, 2016.
- 417
- 418 Robson, J., Ortega, P. and Sutton, R.: A reversal of climatic trends in the North Atlantic since 2005, *Nat.*  
419 *Geosci.*, 9(7), 513–517, doi:10.1038/ngeo2727, 2016.
- 420
- 421 Robson, J., Polo, I., Hodson, D. L. R., Stevens, D. P. and Shaffrey, L. C.: Decadal prediction of the North  
422 Atlantic subpolar gyre in the HiGEM high-resolution climate model, *Clim. Dyn.*, 50(3), 1–17,  
423 doi:10.1007/s00382-017-3649-2, 2017.
- 424
- 425 Sarafanov, A., Falina, A., Mercier, H., Sokov, A., Lherminier, P., Gourcuff, C., Gladyshev, S., Gaillard,  
426 F. and Daniault, N.: Mean full-depth summer circulation and transports at the northern periphery of the  
427 Atlantic Ocean in the 2000s, *J. Geophys. Res. Ocean.*, 117(1), 1–22, doi:10.1029/2011JC007572, 2012.
- 428 Toole, J. M., Andres, M., Le Bras, I. A., Joyce, T. M. and McCartney, M. S.: Moored observations of the  
429 Deep Western Boundary Current in the NW Atlantic: 2004–2014, *J. Geophys. Res. Ocean.*, 1–18,  
430 doi:10.1002/2017JC012984, 2017.
- 431
- 432 Walin, G.: On the relation between sea-surface heat flow and thermal circulation in the ocean, *Tellus*,



433 34(2), 187–195, doi:10.3402/tellusa.v34i2.10801, 1982.

434

435 Wunsch, C.: What is the thermohaline circulation?, *Science* (80-. ), 298(November), 1179–81,

436 doi:10.1126/science.1079329, 2002.

437

438 Yashayaev, I. and Loder, J. W.: Further intensification of deep convection in the Labrador Sea in 2016,

439 *Geophys. Res. Lett.*, 44(3), 1429–1438, doi:10.1002/2016GL071668, 2017.

440

441 Zantopp, R., Fischer, J., Visbeck, M. and Karstensen, J.: From interannual to decadal: 17 years of

442 boundary current transports at the exit of the Labrador Sea, *J. Geophys. Res. Ocean.*, 1–25,

443 doi:10.1002/2016JC012271.Received, 2017.

444